Parameter Optimization in Sea Ice Models with Elastic-Viscoplastic Rheology

Gleb Panteleev[1], Max Yaremchuk[1], Jacob N. Stroh[2], Oceana P. Francis[3], and Richard Allard[1]

[1]Naval Research Laboratory, Stennis Space Center, MS, USA
[2]University of Colorado, Aurora, CO, USA
[3]University of Hawaii, Honolulu, HI, USA

Correspondence: Gleb Panteleev (gleb.panteleevnrlssc.navy.mil)

Abstract. Ice rheology formulation is the key component of the modern sea ice modeling. In the CICE6 community model, rheology and landfast grounding/arching effects are simulated by functions of the sea ice thickness and concentration with a set of fixed parameters empirically adjusted to optimize the model performance. In this study we consider a spatially variable extension of representing these parameters in the two-dimensional EVP sea ice model with a formulation similar to CICE6. Feasibility of optimization of the rheological and landfast sea ice parameters is assessed by applying variational data assimilation to the synthetic observations of ice concentration, thickness and velocity. It is found that the tangent linear and adjoint models featuring EVP rheology are unstable, but can be stabilized by adding Newtonian damping term into the adjoint equation. The set of the observation system simulation experiments shows that landfast parameter distributions can be reconstructed after 5-10 iterations of the minimization procedure. Optimization of the sea ice initial conditions and spatially varying parameters in the equation for the stress tensor requires more computation, but provides a better hindcast of the sea ice state and the internal stress tensor. Analysis of the inaccuracy in the wind forcing and errors in the sea ice thickness observations have shown reasonable robustness of the variational DA approach and feasibility of its application to the available and incoming observations.

1 Introduction

Due to significant decline of the sea ice (SI) volume in the Arctic Ocean in the last decades, the sea ice component of the global climate change becomes a more important factor. Currently, there are several community sea ice models (SIMs) broadly used for modeling and reconstruction of the Arctic Ocean state through various Data Assimilation (DA) algorithms. Many of these models (e.g. Menemenlis et al. 2008; Heimbach 2008; Fenty et al. 2017, Zhang and Rothrock, 2003, Vancoppenolle et al. 2009; Massonnet et al. 2015) are based on visco-plastic (VP) rheology proposed by Hibler (1979). In the last decades, several numerical approaches have been proposed for solving the VP problem (Hibler, 1979; Zhang and Hibler; 1997; Lemieux et al, 2008). These approaches are based on implicit solvers and require a significant number of iterations to achieve full convergence.

Application of more efficient quasi-Newtonian solvers suffers from the lack of robustness and these are usually applied in the SIMs of intermediate resolution (Lemieux et al., 2012; Losch et al., 2014). In addition, implicit VP solvers are not well suited

25   for implementing on the massively parallel supercomputer architectures. Despite these inconveniences the only known 4dVar SIM utilizes an implicit VP solver for time integration of the tangent linear and adjoint (TLA) models (Menemenlis et al. 2008; Heimbach 2008). The Elastic-VP (EVP) rheology was proposed as an alternative explicit method which can be easily adopted for supercomputer architectures (Hunke and Duckowicz, 1997). In addition to the VP parameterization of the internal stress tensor, EVP includes an additional elastic term which requires internal subcycling to dump elastic oscillations in order

30   to achieve the VP solution. The most widely used SIM with EVP rheology is the Community sea ICE model (CICE, Hunke et al., 2010) which is currently maintained and developed by a group of institutions in North America and Europe known as the CICE Consortium. It is widely used in sea ice and coupled sea-ice-atmosphere modeling (Allard et al, 2018; Yaremchuk et al, 2019). There are multiple examples of 3dVar, ensemble-based DA systems utilizing the CICE (e.g., Zhang and Bitz, 2018), but upon our knowledge there is no 4dVar DA system based on the CICE model yet.

35   In the majority of SIMs, the sea ice rheology is defined by three major parameters (P^*, e, and α) describing respectively the dimensional maximum ice strength per unit thickness, the yield ellipse eccentricity, and non-dimensional scaling of ice strength with its compactness. For modeling landfast ice in shallow regions and arching phenomena in the straits, an additional parameter k_T has been introduced to model the tensile strength (Konig Beatty and Holland, 2010). This parameter is absent in the traditional (i.e. Hibler 1979) elliptical yield curve formulation. Lemieux et al, (2015) proposed a number of additional

40   parameters k_1, k_2, α_b, for better parameterization of the landfast ice grounded in the shallow regions. Typically, the above mentioned rheological parameters (RPs) are constants and their values are defined empirically from multiple numerical experiments. RPs such as P^* and e reflect the model parameterization rather than physics and thus directly unobservable (Kreyscher et al. 2000), but are nevertheless known to range within certain limits (Harder and Fischer 1999). As a few examples, the typical values of P^* determined from the sea ice drift were diagnosed to vary within 27.5 kN/m^2 (Hibler III and Walsh, 1982), 15-20

45   kN/m^2 (Kreyscher et al., 1997, 2000), and 30–45 kN/m^2 (Tremblay and Hakakian, 2006). These studies indicate the existence of significant variations of the P^* estimates, which may be attributed to both non-physical considerations (such as spatially variable model resolution), and spatio-temporal variations of the Arctic sea ice. As an example, Tremblay and Hakakian, (2006) introduced a non-elliptic form of the yield curve to improve representation of the SI rheology.

Numerical experiments of Lemieux et al., (2016) with a coarse resolution pan-Arctic CICE-NEMO model have shown that

50    $k_T = 0.2$ provides the best agreement with landfast strength observations in the Kara Sea, when the ellipse eccentricity ranges within 1.2-1.4. The most sensitive parameters for sea ice grounding are the critical thickness parameter k_1 and maximum basal stress parameter k_2. The optimal values were found to be 8 and 15 N/m^3 respectively with higher sensitivity with respect to k_1 (Lemieux et al. 2015). However, the fixed values of k_T, k_1 and k_2 cannot provide a universally good performance of the landfast modeling for different parts of the Arctic Ocean, suggesting that these parameters are the functions of local

55   environmental conditions.

Recently, the impact of spatial non-uniformity of P^* was analyzed by Juricke et al. (2013) who found that a SIM typically generates greater ice volume and lower ice cover area when P^* was stochastically perturbed, and that such effects could not be reproduced using modification of the single value of P^*.

Thus, numerous modeling experiments and sea ice observations (e.g. Toyota and Kimura, 2018) indicate that spatially vary-
ing RPs should significantly improve the sea ice model performance. Feasibility of reconstructing the spatially varying fields of P^* and e through the variational DA of synthetic observations of the Sea Ice Velocity/Concentration/Thickness (SIV/SIC/SIH) was recently analyzed by Stroh et al, (2019) in the framework of the 1d (zonal) VP SIM. It was found that variational DA allows reasonable reconstruction of spatially varying P^* and e in the regions with strong convergence and significantly improves short range hindcast/forecast of the sea ice state. In particular, it was shown that optimization of spatially varying P^* and e provides
more accurate reconstruction of the ridging areas, that cannot be achieved by optimizing initial sea ice state only.

In this study, we extend the investigation to analyize the feasibiltiy of RP optimization within a more advanced 2d SIM based on the EVP rheology formulation of Lemieux et al (2016). Our approach is based on application of the 4-Dimensional Variational Data Assimilation (4Dvar) and Observing System Simulation Experiment (OSSE) concepts (e.g. Nichols 2003, 2010). Similarly to Stroh et al, (2019), we developed the corresponding EVP TLA models and analyzed the feasibility of
the optimization of spatially varying ellipse ratio and sea ice compressive strength. In addition, we also analyzed feasibility of optimizing two of the landfast sea ice parameters introduced by Lemieux et al (2016). Through the multiple OSSEs we evaluate the quality the RP reconstruction and analyze the impact spatially varying RPs on the sea ice state. Similar approach was recently proposed for optimization of the basal stress parameters in the ice sheets model (Goldberg and Heimbach, 2013).

The paper is organized as follows: Section 2 describes the implemented SIM, the details of the TLA codes and generation
of synthetic observations and the first guess solution used in OSSE experiments. Results of these experiments are described in Sections 3 (optimization landfast sea ice parameters) and 4 (optimization compressive strength and ellipse ratio), with special focus on the feasibility of optimizing spatially varying RPs in the context of present and future observational coverage of the sea ice at high latitudes. Section 5 summarizes the work and discusses directions of future research.

2 Sea ice model and its 4dVar implementation

This section provides details of the SIM formulation, its associated linearizations, outlines the variational data assimilation system used for optimization of the model parameters, and describes synthetic observations used to do so. To distinguish between the parameter fields spatially varying in 2d and the fixed parameter values that were not subject to optimization, the latter are marked by tildes. The major parameters of the model are listed in Table 1.

2.1 EVP sea ice model

In the present study, we employed the SIM formulation of Lemieux et al (2016) with the basal stess parameterization and generalized Hibler (1979) yield curve. Equations of the model describe EVP ice physics coupled with SI dynamics which is

forced by the stresses $\boldsymbol{\tau}$ exerted on ice through its interaction with the bottom $\boldsymbol{\tau}_b$ and atmosphere $\boldsymbol{\tau}_a$:

$$\tilde{\rho}hA(\partial_t + \tilde{f}\boldsymbol{k}\times)\boldsymbol{u} = \text{div}\boldsymbol{\sigma} - \boldsymbol{\tau}_b + \boldsymbol{\tau}_a \tag{1}$$

$$\tilde{T}_d\,\partial_t\boldsymbol{\sigma} + e^2\boldsymbol{\sigma} - \frac{e^2-1}{2}\text{tr}\boldsymbol{\sigma}\boldsymbol{I} = P\left[(1+k_T)\frac{\boldsymbol{\varepsilon}}{\Delta} - \frac{1-k_T}{2}\boldsymbol{I}\right] \tag{2}$$

90

$$\partial_t h = \text{div}(h\boldsymbol{u}) \tag{3}$$

$$\partial_t A = \text{div}(A\boldsymbol{u}) \tag{4}$$

Here $\boldsymbol{k}$ is the vertical unit vector, $\boldsymbol{I}$ is the 2×2 identity matrix, h, A, and $\boldsymbol{u} = \{u,v\}$ are the 2d fields of ice thickness, concentration and velocity, and $\boldsymbol{\sigma}$ and $\boldsymbol{\varepsilon}$ are the 2d fields of ice stress and the deformation rate tensors:

$$\boldsymbol{\sigma} = \begin{bmatrix} \sigma_{xx} & \sigma_{xy} \\ \sigma_{xy} & \sigma_{yy} \end{bmatrix}; \quad \boldsymbol{\varepsilon} = \frac{1}{2}\begin{bmatrix} 2\partial_x u & \partial_x v + \partial_y u \\ \partial_x v + \partial_y u & 2\partial_y v \end{bmatrix} \tag{5}$$

95   The scalar field Δ used for normalization of ε is given by the following expression (e.g., Hunke, 2001):

$$\Delta(\boldsymbol{\varepsilon}) = \frac{1}{e}\left[(1+e^2)(\text{tr}\boldsymbol{\varepsilon})^2 - 4\text{det}\boldsymbol{\varepsilon}\right]^{1/2} \tag{6}$$

To avoid numerical singularities at $\boldsymbol{\varepsilon} = 0$, the values of Δ are limited from below by the additional parameter $\tilde{\Delta}^* = 10^{-10}\ \text{s}^{-1}$, so that $\Delta(\boldsymbol{\varepsilon}) = \max(\Delta, \tilde{\Delta}^*)$.

The empirical parameters $\tilde{T}_d, P, k_T$ and e in equations (1)-(4) define the elastic damping scale of sea ice, its internal pressure,

100   isotropic tensile strength, and the yield curve eccentricity respectively.

The internal ice pressure P is related to ice thickness and concentration in accordance with Hibler's (1979) SI rheology: for P:

$$P = P^* h A \exp\left[-\tilde{\alpha}(1-A)\right] \tag{7}$$

The typical values of the ice strength parameters P^*, $\tilde{\alpha}$ are listed in Table 1.

105   The basal stress $\boldsymbol{\tau}_b$ in eq. (1) was parametreized in accordance with Lemiuex et al. (2015; 2016):

$$\boldsymbol{\tau}_b = \Theta(h - Ah_b/\tilde{k}_1)\frac{k_2\boldsymbol{u}}{|\boldsymbol{u}| + \tilde{u}_0}\exp\left[-\tilde{\alpha}_b(1-A)\right] \tag{8}$$

where Θ is the Heavyside step function, h_b is the ocean depth, $\tilde{\alpha}_b = 10$, $u_0 = 10^{-5}$ m/s, $\tilde{k}_1 = 8$, and k_2 is the adjustable parameter field (see Table 1).

In contrast to the previous studies, where the free empirical parameters P^*, e, k_T and k_2 were assumed to be constant,

110   the present study attempts to retrieve their spatial variability from simulated (satellite) observations of the SI state vector $\boldsymbol{C} \equiv \{h, A, \boldsymbol{u}\}$ using variational DA technique.

2.2   Adjoint and tangent linear models

Following Lemieux et al (2016), SIM equations were discretized on the Arakawa B-grid and integrated forward in time using a two-stage Euler time stepping. At the first stage, the fields of velocity $\boldsymbol{u}$ and ice stress $\boldsymbol{\sigma}$ were advanced in time using a

Table 1. Model and assimilation system configuration parameters

Constant parameters		
Name	**Symbol**	**Value**
Coriolis parameter	$\tilde{f}$	10^{-4} s^{-1}
Ice density	$\tilde{\rho}$	900 kg m^{-3}
Advective time step	δt	600 s
Subcycling time step	δt_s	1.5 s
Elastic damping scale	$\tilde{T}_d$	15 s
Creep limit	$\tilde{\Delta}^*$	10^{-10} s^{-1}
Compactness strength parameter	$\tilde{\alpha}$	20
Compactness basal stress parameter	$\tilde{\alpha}_b$	20
Critical thickness parameter	$\tilde{k}_1$	8
Controlled parameter fields		
Name	**Symbol**	**Range**
Base Strength Parameter	P^*	$22 - 33$ kN/m^2
Yield curve eccentricity	e	$0.9 - 3.1$
Tensile/Compressive Strength ratio	k_T	$0 - 0.8$
Maximum basal stress parameter	k_2	$0 - 20$ N/m^3

115 "subcycling time step" δt_s=1.5 s to obtain the velocity values at the end of the advective time interval $dt = 600$ s, and then the fields of ice concentration A and thickness h were updated using the explicit advective time step in equations (3)-(4).

The TLA codes was derived by analytic differentiation of the above mentioned numerical scheme in the vicinity of a background model trajectory and transposition of the code simulating the action of the TL matrix on a perturbed state vector. The most laborious part in deriving the TLA codes was associated with linearization of the rhs in eq. (2) with respect to ice veloci-
120 ties. Note that the first term in the rhs of the linearized eq. (2) is proportional to the first derivatives of the velocity perturbations $\delta\boldsymbol{u}$. As a consequence, the components of $\boldsymbol{\sigma}$ are linear in the first derivatives of $\delta\boldsymbol{u}$ after taking the explicit time step δt_s in the linearized eq. (2). Moreover, the first-order derivatives in $\boldsymbol{u}$ keep their presence in the rhs of the linearized eq. (1) due to spatial variability of the background fields in equations (6) and (7).

This property of the TL equations of the subsystem (1)-(2) may require additional care in the specification of the subcycling
125 time step δt_s because the gradients of the background fields of h and A may invoke considerably larger propagation speeds of the effective elastic waves than those present in the original non-linear model. Consequently, the TL code could be constrained by a more stringent stability criterion and require even smaller subcycling time steps than those used in the integration of the full non-linear model. In particular, the non-linear stability criterion could be violated, for example, in the areas of strong ice convergence where the background field is characterized by the large values of SIT gradients which may cause, as it follows
130 from (7) large coefficients before the first-order derivatives of $\delta\boldsymbol{u}$ in the TL code of the second term in the rhs of eq. (2).

Preliminary numerical experimentation with the TL code demonstrated a necessity to reduce δt_s as the TL solutions demonstrated uncontrollable amplification of velocity perturbations over the areas of strong sea ice convergence in the background fields. Our attempts to reduce δt_s by an order in magnitude reduced this type of amplification with a limited success. Martin Losch observed similar instability of the TL EVP solver in the MIT SIM (personal communication).

135 Instability of the linearized codes in the strongly non-linear regimes of the parent model is a well known phenomenon in the ocean general circulation models (OGCMs). A heuristic solution of the problem was proposed by Hoteit et al, (2004) who added extra diffusion in TLA codes to suppress unstable small-scale harmonics. This kind of treatment is achieved, however, at the expense of the reduction of the TLA code accuracy (e.g., Yaremchuk et al, (2009)). Later, Yaremchuk and Martin, (2014) established a connection between the length of the DA window and the magnitude of the diffusion tensor in the TLA

140 regularization trems.

However, in the SIM considered, this type of regularization did not work even when the contribution of the stabilization term was comparable in magnitude with the contributions from other terms in the TLA codes. We attribute this phenomenon to the specific structure of the unstable modes in the TL equations, which often take the form of elongated ridge-like structures (i.e. have a wide spatial spectrum) in the areas of ice convergence. As a consequence they cannot be efficiently damped using an

145 isotropic diffusion tensor in the TL momentum equations. A straightforward solution is to introduce spatially inhomogeneous diffusion tensor field (e.g. Yaremchuk and Nechaev, 2013), with local anisotropy derived from the background solution. However, this would require a considerable reduction of δt_s due to very large diffusion along the ridges. As a simple alternative, we tried more simple Newtonian friction term, which homogeneously damps the entire spectrum of small perturbations. Numerical experimentation has shown that this approach worked generally well using Newtonian damping time scale τ_d of 3–5δt_s.

150 Additional experiments have shown that τ_d has to be decreased to 4δt_d in the cases of stronger SI convergence in the regions with thick ($h > 3$ m) ice.

Testing the validity of the stabilized TLA codes was done in a way similar to Yaremchuk et al, (2009). The initial conditions for the SIM's thickness and concentration fields $\boldsymbol{C} = \{h(\boldsymbol{x},0), A(\boldsymbol{x},0)\}$ were slightly perturbed by the realizations of a random function R (viz. $\boldsymbol{C}(\boldsymbol{x},0) \to \boldsymbol{C}(\boldsymbol{x},0) + \epsilon R(\boldsymbol{x}) \equiv \boldsymbol{C} + \delta \boldsymbol{C}$), and the model and its TL version were integrated for $t = 5\delta t$. After

155 that, the dependence of the normalized diffrence between the non-linear solution and its TL approximation was checked by computing the following quantity:

$$\Phi(\epsilon) = \frac{|N(\boldsymbol{C} + \delta \boldsymbol{C}) - N(\boldsymbol{C}) - TL(\delta \boldsymbol{C})|}{|N(\boldsymbol{C})|} \tag{9}$$

where N is the state vector of the non-linear model at time t generated by the initial conditions listed in the argument, and $|\cdot|$ is the euclidean norm. As it is evident from Fig. 1, the stabilized version of the TL code is charactrized by $\Phi(\epsilon) \propto \epsilon$, while the

160 correct TL code should provide the decay proportional to the square of ϵ. Decay of Φ for the unstable TL code is slightly faster than the stabilized one, but the respective solutions produce very noisy patterns causing much earlier stagnation of the descent process as compared to the stabilized code.

It is noteworthy, that behavior of $\Phi(\epsilon)$ in the similar experiments with 1d VP SIM (Stroh et al, 2019) agreed well with the ϵ^2 dependence of the Taylor expansion (blue line in Fig. 1). We speculate that, similar to the 1d case, stability criteria of the 2d VP
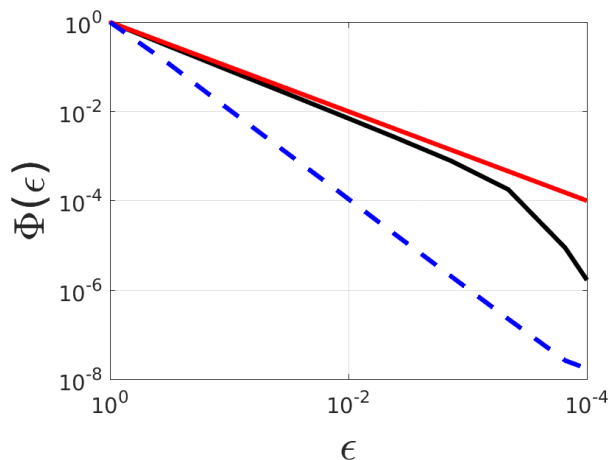
Figure 1. TL approximation errors $\Phi(\varepsilon)$ of the EVP (black), regularized EVP (red), and VP SIM (blue dahed) solutions.

system may also be weakly affected by the TL transition due to the specific nature of the linearization in the implicit momentum equation solver (see Appendix). These considerations may indicate an additional attractive feature of the VP rheology in the practical 4dVar applications.

In the OSSE experiments described below, the control variables included initial conditions for sea ice velocity, thickness and concentration, the wind stress and the spatially varying RP fields of P^*, e, k_T, and k_2. For other other RPs we utilized constant values adopted from Lemieux et al., (2016) and listed in Table 1.

2.3 Simulated observations and cost functions

In all OSSE experiments we used three types of simulated sea ice observations. The first type of data are accurate SIC observations, of which there are currently multiple gridded products based on various remote sensing instruments with different spatial resolutions. After additional pre-processing, these observations are routinely used in data assimilation systems (e.g. GOFS 3.1 DA system of Cummings and Smedstad, (2013)), with a nominal spatial resolution of 5 km and regionally low SIC representation errors (5%, Yaremchuk et al. 2019).

The second data type are SIT observations which contain moderate errors. Currently, the primary source of such data is CryoSat-2, with 1 km and 5 km gridded 2-day averaged observations available from the Center for Polar Observations and Modeling (*http://www.cpom.ucl.ac.uk/csopr/seaice.html*). Currently, the error estimates of CryoSat-2 SIT observations range between 0.34–0.74 m (Alexandrov et al., 2010, Laxon et al. 2013, Tilling et al. 2018). The recently launched Icesat-2 satellite provides high resolution (40m) freeboard estimates *https://icesat-2.gsfc.nasa.gov/* with higher accuracy. So, in the future, novel observational platforms and methods of analysis will likely provide better spatial coverage (i.e. over the entire Arctic) and improved accuracy. In the experiments, we set SIT observation errors of 0.3 m, having in mind future improvements of the SIT data accuracy. Similar error level was adopted by Stroh et al, (2019), who studied RP retrievals in a 1d SIM.

Table 2. List of the experiments

Experiment	Grid size and resolution δx	Description	Objective	Control fields
KT	70×7, 15 km	zonal wind forcing, true k_T=0.6	Evaluate feasibility of optimizing k_T in narrow straits.	k_T, h_0, A_0
K2	75×30, 15 km	zonal wind forcing, true k_T=15, sloping bottom topography	Evaluate feasibility of optimizing k_2 in shallow seas	k_2
GYRE-0, GYRE-W	75×30, 30 km	True solution with cyclonic wind forcing and spatially varying P^*, e	Evaluate feasibility of optimizing P^*, e in central Arctic under correct and biased wind forcing shallow sea.	P^*, e, h_0 A_0,
PIZ	75×30, 30 km	Truie solution with convergent wind forcing and spatially varying P^*, e	Evaluate feasibility of optimizing P^*, e in PIZ areas under convergent winds	P^*, e, h_0, $\boldsymbol{u}_0$,

185   Accurate observations of sea ice velocities compose the third data type. An example product is the daily 25 km SIV analysis of various satellite and in situ sources (Tschudi et al. 2019). The respective uncertainties were established at 0.01–0.02 m/s level (Schwegmann et al. 2011; Sumata et al. 2015). New methods of sequential SAR image comparison can resolve high-resolution SIV with an accuracy of 0.005 m/s (Komarov and Barber 2014), suggesting a possibility of high-precision SIV observations in the near future. In the OSSEs reported below, inaccuracy of SIV is set to 0.01-0.025 m/s.

190   Simulated SIC, SIV and SIT observations were derived from the "true" solution with spatial decorrelation scale of 150 km and temporal decorrelation scale of 7 days. Taking into account that high resolution satellite SIC, SIV are currently available on a daily basis over the entire Arctic Ocean and assuming they can be interpolated within every daily time frame, we set synthetic observations to be available in all the space-time grid points ($600{\times}8990 \approx 5.4 \cdot 10^6$) of the model domain.

    The standard 4Dvar DA approach of Le Dimet and Talagrand (1986) wass utilized: the optimal vector $\boldsymbol{C}$ of control variables
195 was sought to ensure that observations of the model states lie close to assimilated observations within the prescribed time interval (assimilation window) which was set to 3 days in all the experiments. The DA procedure was performed by minimizing the quadratic cost function $J(\boldsymbol{C})$ which included simulated data and regularization (smoothness) terms both characterized by the diagonal error covariance matrices. In addition, we applied bounding constraints on the field values of ice concentration ($0 \leq A \leq 1$), and the control fields of the rheological parameters (listed in the bottom of the left column in Table 1).

200 ## 2.4   OSSEs

    The major goal of the conducted OSSEs was to evaluate the feasibility of reconstructing the RPs through assimilation of the SIV, SIC and SIT observations. The first group of the OSSEs analyze the feasibility of optimizing landfast ice parameters k_2 and k_T. In the second group, we analyzed feasibility of optimizing P^* and e in the regions with spatially and temporally varying SIT and SIC. In the third group, we analyzed feasibility of optimizing P^* and e in the pack ice zone (PIZ) with
205 spatially varying SIT and fixed SIC equal to 1. We also analyze the impact of the P^* and e optimization on the hindcast of ice

thickness and internal stress distributions. A list OSSEs and with short descriptions is assembled in Table 2. The RP control fields were defined on coarser (δx_p=7(or 15)δx) grids with bilinear interpolation on the SIM grid of the respective OSSEs. In all the experiments we assumed that SIT, SIC and SIV observations were available in all the space-time grid points of the model domain.

3 Optimization of the landfast parameters

3.1 Arching: opimization of k_T

Formation of the landfast ice (LFI) in the deep narrow straits and between islands is a well known phenomenon in the Canadian Archipelagos and in the Kara Sea (e.g. Lemieux et al, 2016). In the Nares Strait, LFI is observed periodically and typically its boundary has an arching shape (e.g. Ryan and Munchow, 2017).

To mimic this phenomenon, the SIM was configured in the relatively narrow zonal domain and forced by the steady 10 m/s wind for 3 days (Figure 2a). The initial values of the SIT/SIC fields were set constant with respectively 2m/1.0 and 0.2m/0.7 values in the western and eastern parts of the domain. Zero initial velocities and the tensile/compressive strength ratio k_T=0.6 were used to obtain the "true" solution (Figure 2a). Figure 2b shows, that after 3 days the sea ice in the western part of the domain did not drift eastward due to internal tensile strength, which was strong enough to keep sea ice in place, i.e. forming the LFI area in the western part of the domain. Since in the eastern part the tensile strength was weaker due to thinner (0.2 m) ice and smaller SIC (0.7), sea ice moved eastward with typical velocities of about 0.1 m/s forming the polynya between the LFI area and thinner sea ice.

The first guess solution was forced by the same wind but with k_T=0 using disturbed initial SIT and SIC fields. Figure 2c shows the first guess state at the end of the assimilation window (t=3 days). It is clearly seen that SI moved eastward with a speed of 0.1–0.15 m/s throughout the entire domain, with the sharp boundary between thick and thin ice (Fig. 1a) deteriorating and the 10km wide polynya developing at the western boundary. The LFI area is completely absent in this solution where ice has no tensile strength (k_T=0).

The 4dVar optimization of only k_T (initial distributions of SIC and SIT were not optimized) provides a significant improvement of the SIC and SIT (not shown) clearly seen in Figure 2d. The optimized k_T is shown in Figure 2f and is very close to the true (0.6) value almost everywhere in the western part of the domain while in the eastern part it is close to zero. Thus, the optimization of k_T enabled formation of the LFI area in the western part of the model domain. Obviously, a similar effect could be achieved with much higher values of k_T. To remove this ambiguity, we added an additional term $\omega \int k_T^2(x)dx$ into the cost function, minimizing the integral values of k_T in an attempt to find the minimum value of k_T necessary for holding ice in place. Note, that optimization was achieved in only four iterations (Figure 2e), which is the result of the small dimension of the k_T control vector due to sparse representation of the RPs in 4dVar DAS. It is also possible to optimize the initial SIT and SIC in addition to k_T. This kind of the optimization provides better SIT/SIC hindcast but requires more iterations to find the minimum (Figure 2e).
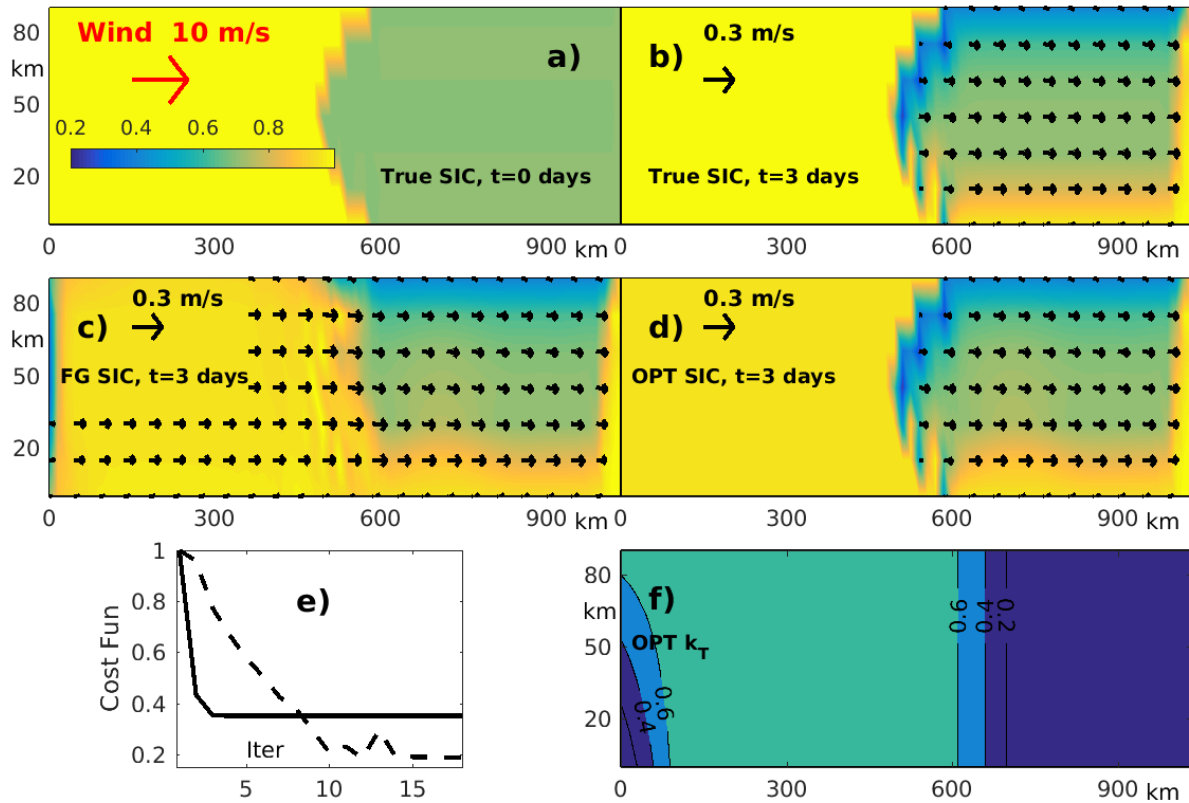
Figure 2. Results of the OSSEs optimizing k_T: *Top panels:* True SIC and SIV with k_T=0.6 at t=0 (a) and t=3 days (b). *Middle panels* The first guess (c) and optimized (d) SIC and SIV fields at t=3 days; *Bottom panels:* evolution of the normalized cost function for the OSSE with optimization of k_T only (solid line) and with the joint optimization of k_T, h, and A (dashed line). Left panel shows the optimized k_T distribution.

3.2 Grounding effect: opimization of k_2

Grounding on the shallows is another mechanism of LFI formation. This kind of the LFI is typically observed in the Laptev,

240 Chukchi and East Siberian seas and along the northern Alaskan coast (e.g. Lemieux et al, 2015). To mimic this phenomenon, the SIM was configured in the rectangular 1125×450 km domain (Figure 3) with zonally varying depth ranging between 3m at the western boundary and 33 m at the eastern boundary (Figure 3e). The model was forced by the uniform 10 m/s wind. The true solution was specified as follows. The initial SIC ranged between 0.2 and 1 while the initial SIT was proportional to the SIC and ranged between 0.25m and 2.5m as shown in Figure 3a. Initial velocities and the tensile/compressive strength ratio k_T,

245 were set to zero, while the following values of the RPs were used: the critical thickness parameter $\tilde{k}_1$=8, basal stress parameter $\tilde{\alpha}_b$=10, the and maximum basal stress parameter k_2=16 N/m^3. Figure 3b shows that after 3 days the sea ice moved eastward in
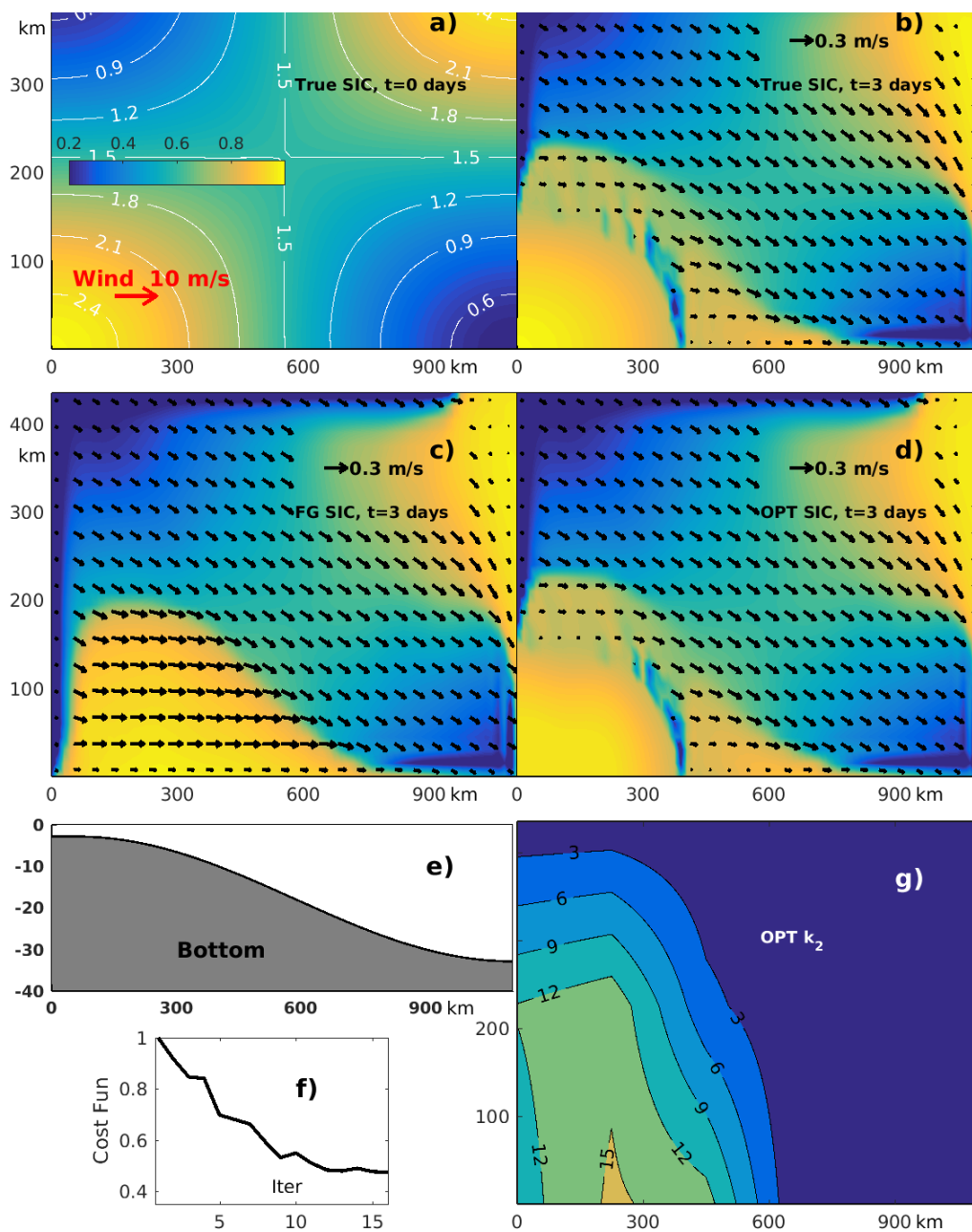
Figure 3. Results of the k_2 optimization: *Upper panels:* True SIC and SIV with k_2=15 at t=0 and t=3 days respectively. SIT distribution (meters) is shown by white contours in the left panel; *Middle panels:* The first guess SIC and SIV with k_2=0 at t=3 days (c) and (d) optimized SIC and SIV at t=3 days. *Bottom panels:* zonal topography profile (e), evolution of the normalized cost function for the OSSE with optimization k_2 (f), and the optimized k_2 distribution (g).

the most regions with typical speed about 0.2-0.4 m/s and only in the south-western corner the combination of the SIT, SIC, and bottom topography was sufficient to keep sea ice in place, thus forming the region of grounded LFI. Another interesting feature is the elongated polynya along the eastern boundary of the LFI region visible in Figure 3b.

250   The first guess solution had the same parameters with the exceptions of k_2, SIV (both set to zero) and the slightly disturbed initial SIT and SIC fields as shown in Figure 3c. It is clearly seen that wind forcing moves sea ice eastward with a speed of 0.3-0.4 m/s, forming a polynya along the western boundary which does not exist in the true solution and the LFI area in the southwestern corner is completely absent. The above mentioned polynya separting the LFI from the moving ice in the south (bottom of Figure 3b) is also absent in the first guess solution.

255   The variational assimilation of the SIV, SIC and SIT observations to optimize only k_2 (similar to the KT experiments initial SIC and SIH were not optimized) demonstrates a significant improvement of the SIC and SIT (not shown) clearly seen in Figure 3d. The optimized field of k_2 is shown in Figure 3g. The maximum values of k_2 are very close to the "true" k_2=16 N/m^3. Note, that the true k_2 value was specified ad hoc and the grounding effect formally could be reached with smaller values of k_2. This is clearly demonstrated in Figure 3g, where k_2 is about 12 N/m^3 over the major part of the LFI area in true solution 260   (cf. Figure 3b,g).

Similar to the KT experiment, the additional term, penalizing the magnitude of k_2 was added to the cost function, and the optimized field of k_2 was obtained after a relatively small number of the iterations (10-12) (Figure 3f). Note also, that according to equations (1) and (8), sea ice acceleration is directly proportional to k_2 which should invoke faster convergence of the minimization procedure.

265   The parametrization of the grounding LFI also includes the critical thickness parameter $\tilde{k}_1$=8, which was kept fixed in the described experiment. According to multiple numerical simulations, the total LFI area is more sensitive to variations of k_1 than k_2 (Lemieux et al, 2015) because $\tilde{k}_1$ can be interpreted as a scaling coefficient in the definition of the critical ice thickness $\tilde{k}_1 h_c = A h_b$ (cf. eq. 8), and works as a "switch" which defines the areas of potential LFI generation. However, the discontinuity of the Heaviside step function present in (eq. 8) significantly complicates k_1 optimization through the gradient- 270   based variational method. Formally, this problem can be regularized (e.g., Nicolsky et al., 2009), but this approach needs an additional "external" optimization with respect of the additional regularization parameter. In practice, this approach could be computationally inefficient. In light of this consideration, we limit our study with analysis of the feasibility of the LFI parameterizations to optimizing k_T and k_2.

4 Optimization of the ice strength and ellipse eccentricity fields

275 ### 4.1 Cyclonic gyre experiments (GYRE-0/W)

The rheological parameters P^* and e are the most important set of the parameters responsible for proper sea ice modeling in the deep part of the Arctic Ocean. To evaluate feasibility of optimizing P^* and e, the EVP model was configured for a 2250 x 900 km rectangular domain with initial true values of the SIC and SIT fields as shown in Figure 4a. The true values of P^* and e varied as shown in Fig 4.e,f within the following ranges: 22.5 kN/m^2 ≤ P^* ≤ 32.5 kN/m^2 and $1 ≤ e ≤3$. These
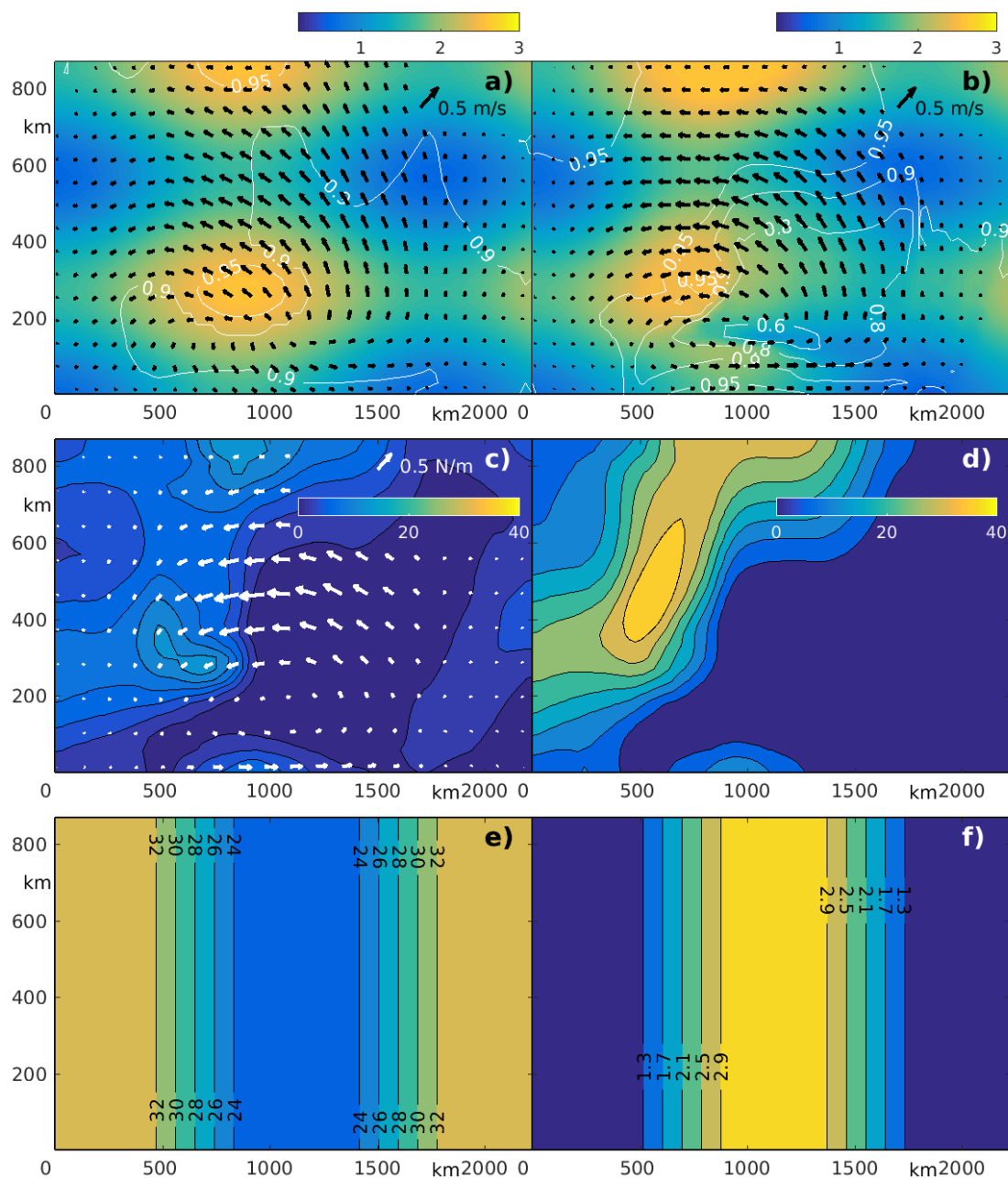
Figure 4. True solution in GYRE-0/W-OSSEs: (a-b) evolution of the SIH, SIC (white contours) and SIV (black arrows) at t=0 (left panel) and 3 days; (c-d) evolution of the trace P_{tr} of the internal stress tensor at t=0 (left) and 3 days. White arrows show the initial wind stress caused by specified cyclonic wind forcing; (e-f) true distributions of P^* (kN/m^2, left panel) and e.

280   ranges were adopted from various studies (e.g. Hibler and Walsh, 1982; Kreyscher et al. 1997, 2000; Tremblay and Hakakian 2006; Lemieux et al. 2016). The true wind forcing had a form of the Gaussian-shaped cyclone with stationary position whose strength gradually increased by 1.5 times during the 3-day assimilation window. The resulting wind stress at t=0 is shown in Figure 4c and had the maximum value of 0.7 N/m^2. Initial SIV conditions were determined by a 100 minute SIM integration starting from rest with the all other initial variables and parameters being the same. The initial internal stress was small, but

285   significantly increased after 3 days under the applied atmospheric forcing. Figures 4c-d show the trace of the stress tensor $P_{tr} = -\mathrm{tr}\boldsymbol{\sigma}/2$ at the beginning of the true state integration and after 3 days. The P_{tr} distribution has a clear maximum near the location with the coordinates (500 km, 500 km), which corresponds to the maximum pressure ($\sim$40 kN/m^2) in the sea ice field (e.g. Tremblay and Mysak, 1997). This maximum is due to strong convergence of the relatively thick (2.5m) sea ice in this region. In the eastern part of the domain, P_{tr} is typically very low due to the divergence of the SIV and considerably thinner

290   (0.5-1.5m) sea ice.

    Noisy SIC, SIT and SIV observations were generated by adding spatially and temporally correlated noise (with the correlation scales of 150 km and 7 days) to each of the state variables of the true solution at every timestep. The simulated data mimics realistic observations such as those obtained from sources discussed in section 2c. The magnitudes of the imposed noise correspond to the errors of the respective observational data sets, with the amplitudes of 0.05, 0.25–0.35 m, 0.025 m/s,

295   and 0.01–0.025 N/m^2 for SIC, SIT, SIV and wind stress respectively. The initial conditions for the first guess solution were generated in a way similar to the true solution, with slightly larger decorrelation length scales for SIT, SIC and SIV and spatially uniform values of P^*=27.5 kN/m^2, e=2 and true wind forcing.

    Despite the exact wind forcing, the first guess solution differs significantly from true solution. Similarly to Stroh et al, (2019), the optimization was conducted in two steps. First, we optimized initial SIV, SIT and SIC conditions $\boldsymbol{C}_{ic} = \{\boldsymbol{u}_0, h_0, A_0\}$. Then

300   we sequentially optimized rheological components of the control vector $\boldsymbol{C}_{rh} = \{P^*, e\}$ and finally conducted an additional optimization of the full control vector $\boldsymbol{C} = \{\boldsymbol{C}_{ic}, \boldsymbol{C}_{rh}\}$.

    Figure 5a-d compares the model states after optimization of the initial conditions $\boldsymbol{C}_{ic}$ with fixed P^* and e (left panels) and after additional spatial optimization of the P^* and e (right panels). The major result of optimizing $\boldsymbol{C}_{rh}$ is an improvement of the SIV fields. The formal quantitative measure of the SIV improvement was evaluated by the function

$$S_{\boldsymbol{u}} = \sum_{\Omega,k} |\boldsymbol{u}_{opt}^k - \boldsymbol{u}_{true}|$$

where Ω is the model domain and index k=1,2 enumerates sub-optimal optimization stages: $k = 1$ using the initial conditions control vector $\boldsymbol{C}_{ic}$ only, and $k = 2$ employing of the full control vector $\boldsymbol{C} = \{\boldsymbol{C}_{ic}, \boldsymbol{C}_{rh}\}$. It was found that $S_{\boldsymbol{u}}$ reduced almost 1.5 times after the additional optimization of the rheological parameters $\boldsymbol{C}_{rh}$ (Figure 5a,b). Visual comparison of the sub-optimal

305   and fully optimized SIC shows a certain improvement after $\boldsymbol{C}_{rh}$ as well. For example, the local minimum of the sub-optimal SIC in the region with coordinates 700-1500 km and 180 km is about 0.7 (white contours in Figure 5a), while the fully optimized SIC has a minimum of 0.6 which is agrees perfectly with the true SIC distribution (white contours in Figure 4b).

    In this experiment we found that optimization of $\boldsymbol{C}_{rh}$ yields only a marginal improvement of the SIT distribution. In particular, $std(h_{opt}^k - h_{true})$ decreased from 0.23 m after optimization of the initial conditions to 0.2 m after additional $\boldsymbol{C}_{rh}$
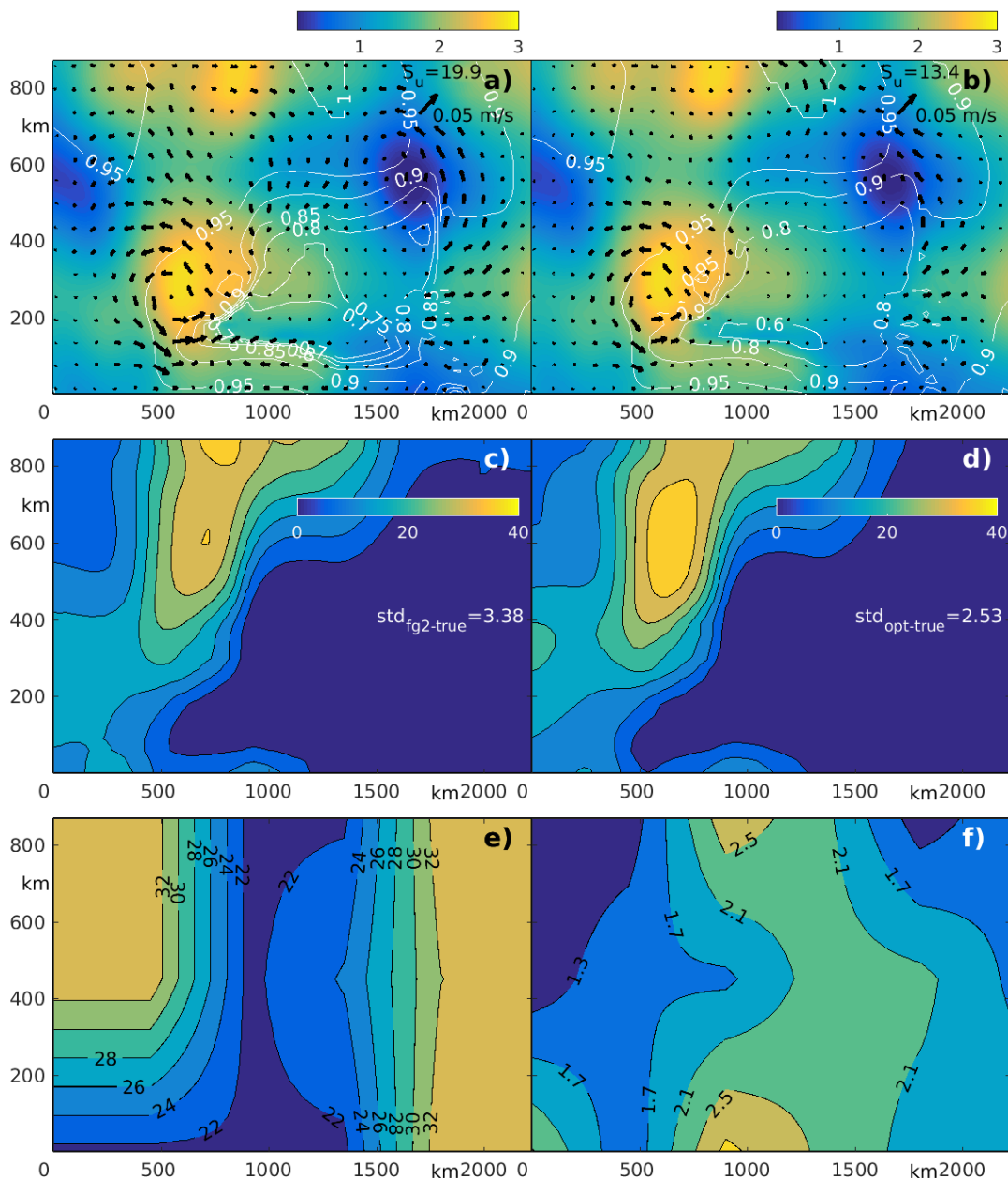
Figure 5. Results of the GYRE-0-OSSE: sub-optimal distribution of SIH, SIA (a) and P_{tr} (c) for t=3 days after optimization of the initial conditions $\boldsymbol{u}_0$, h_0, A_0 using the first guess values of P^*=27 kN/m^2 and e=2. The deviation norms $S_{\boldsymbol{u}}$ and S_{tr} are shown. (b,d) same as (a,c) but after additional optimization of P^* and e; (e,f) – optimized distributions of P^* (kN/m^2) and e. Black arrows in (a,b) show the difference between optimized and true SIV.
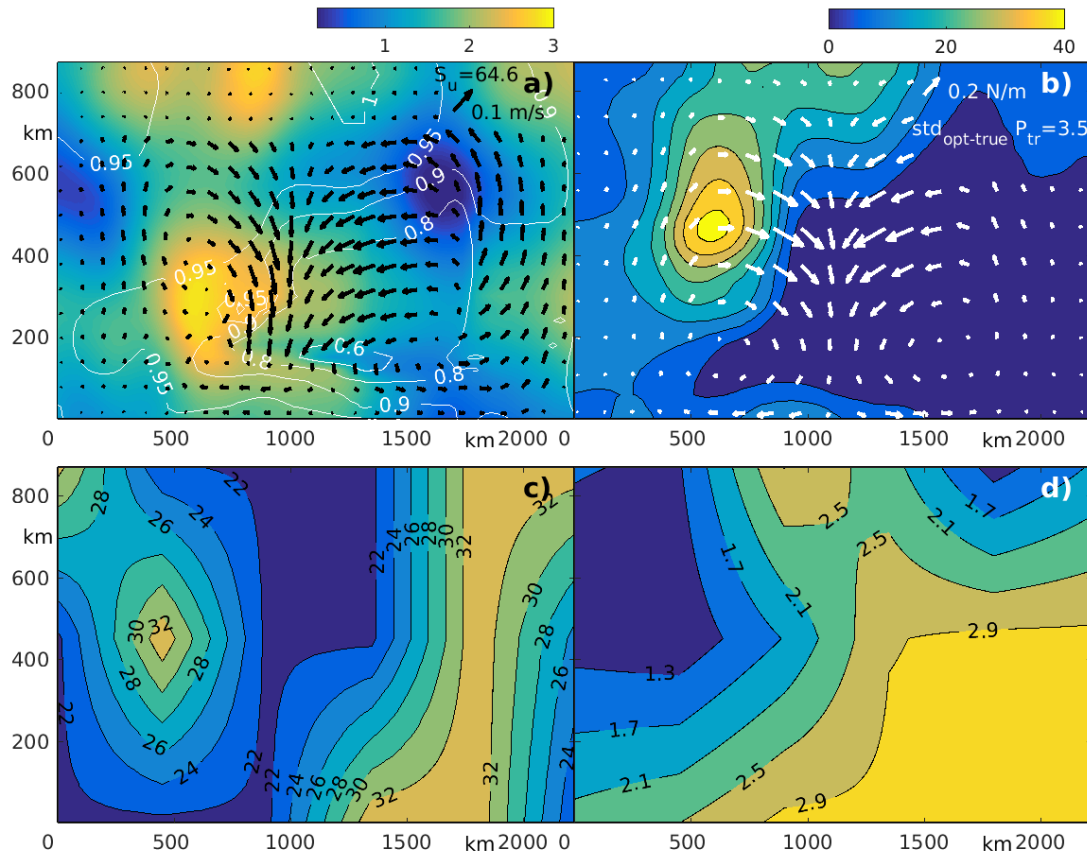
Figure 6. Results of the GYRE-W-OSSE: optimized distribution of SIT, SIC (a) and P_{tr} (b) at t=3 d. Black/white arrows show the differences between true and optimized SIV (a) and wind stress (b) respectively; (c,d) – optimized distributions of P^* (kN/m^2, left) and e.

310 optimization. The minor impact of $\boldsymbol{C}_{rh}$ optimization on the SIT is probably due to relatively high SIT errors and substantial difference between the first guess and observed SITs.

In contrast, optimization of the rheological parameters $\boldsymbol{C}_{rh}$ provides the major impact on the optimization of the internal stress tensor. Figures 5c,d, show that standard deviation of the differences between the true and the optimized values of P_{tr} decreased by 35% after the additional optimization of the RPs. Note also, that the maximum value of fully optimized P_{tr}

315 (Figure 5d) is located in the close proximity of the true P_{tr} maximum (Figure 4d), while the maximum in sub-optimal P_{tr} is shifted almost 400 km northward. Comparison with true P^* demonstrates that the optimized field agrees well with true P^* almost everywhere with the only exception observed in the southeast corner of the domain (Figure 5e). This is due to mean eastward SIV accompanied by divergence of the of the sea ice in course of SIT evolution during the DA window. The reconstruction of e is not as accurate, as P^* with the extreme values of the optimized e being 1.2 and 2.8, while the respective

320 true values are 1 and 3. Note, however, that spatial locations of extrema agrees well with true distribution. The exception is the

local minimum in the south-western corner, where both e and P^* disagree with true values significantly. Note, that significant improvement of P_{tr} and the internal stress components discussed above are directly related to the more accurate optimization of the RP and SIV fields because both P^* and e control the structure of the stress tensor in eq. (2).

325   To analyze impact of the inaccuracy in the wind forcing we conducted an additional experiment where the center of the cyclonic disturbance was displaced 90 km westward mimicking a systematic error in the hypothetical atmospheric forecast. The results obtained after full optimization of the control vector $\boldsymbol{C} = \{\boldsymbol{C}_{ic}, \boldsymbol{C}_{rh}\}$ are shown in Figure 6. It is noteworthy, that inaccurate position of the atmospheric cyclone causes significant errors (up to 0.2 N/m^2, or 25%) in the wind stress forcing in the central part of the domain (Figure 6b). As a result, the optimized SIV fields have essential (0.1 m/s) errors (Figure 6a) and the integral measure of the SIV inaccuracy $S_{\boldsymbol{u}}$ increased five times up to 0.64 m/s.

330   At the same time, degradation of the SIH retrieval was not as significant, with a $std(h_{opt}^k - h_{true})$ increase up to 0.25 m, i.e. only by 25% as compared to the previous experiment with exact wind forcing. Similarly, the optimized SIC distribution remained largely unchanged. The integral quality of the reconstruction of P_{tr} is 3.5kN, i.e. about 40-50% worse than in the experiment with exact forcing, but it is important to note that the maximum in the P_{tr} is still in a very good agreement with the true solution.

335   Although inaccurate wind forcing has a profound impact on the accuracy of P^* and e retrievals, there is still an essential level of similarity between the reconstructed and true rheological fields. For example, spatial distribution of the optimized P^* still has maxima in the western and eastern parts of the region and a minimum in the center of the domain (Figure 6c), while the minimum of the e in the western part agrees well with true e distribution (Figure 4e,f). Note, that inaccurate wind forcing affects the accuracy of P^* retrievals to a less degree than e.

340   ## 4.2   PIZ-OSSE

In both experiments described in the previous section, the initial true SIC was rather close to 1 and decreased to 0.8 in some regions after 3 days of integration (Figure 4a,b). Due to the exponential dependence of P on $1 - A$, (eq. 7) internal stress decreases $\exp(4) \approx 50$ times, and therefore has a minor rheological impact of the sea ice dynamics. At the same time in winter, most of the Arctic Ocean is almost completely covered by pack sea ice with SIC ranging between 0.98 and 1. To mimic these

345   conditions, we conducted another OSSE with spatially and temporally invariant sea ice concentration A=1. Numerically this was achieved by removing the advection equation from eq. (4), and removing initial A_0 from the control vector $\boldsymbol{C}_{ic}$.

The model domain, initial SIT, and P^* and e distributions were the same as in GYRE-0/W-OSSEs. However, unlike the cyclonic wind of the previous experiment, the atmospheric forcing is applied as a 20 m/s eastward wind at the western boundary which reverses zonal direction across the breadth of the domain (fig7c). In time, the wind speed was amplified 1.5 times (to 30

350   m/s) by the end of the DA window. The resulting wind stress at t=3d is shown in Figure 7c and has the maximum amplitude about 0.5 N/m^2.

The temporal evolution of the true SIT and SIV is shown at Figure 7a,b. Under the applied relatively strong wind forcing, sea ice converges and SIH increases over almost everywhere with an exception of the narrow bands along the western and northern boundaries, caused by the joint effect of the Coriolis force and coastal boundary conditions. The true SIV has a maximum of
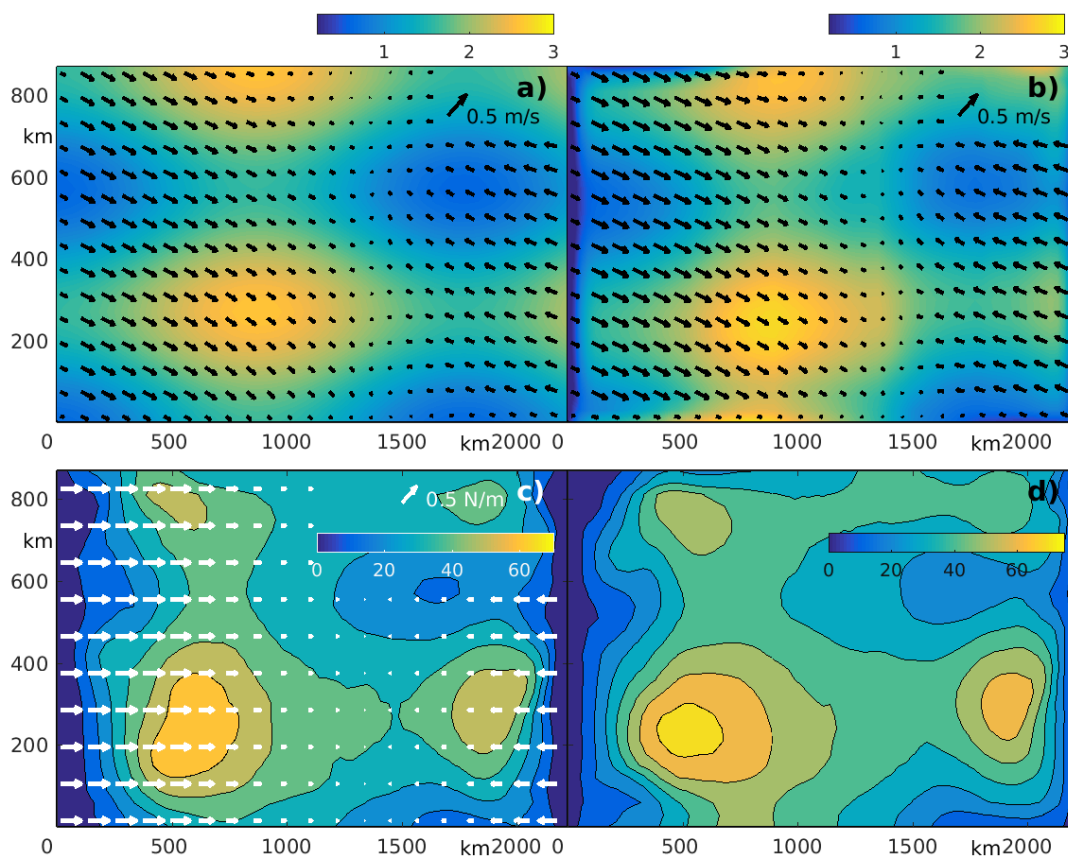
The Cryosphere
Discussions

Figure 7. True solution in PIZ-OSSEs: a-b) Evolution of the SIH and SIV (black arrows) at t=0 (left) and 3 days; c-d) evolution of the P_{tr} of the internal stress tensor. White arrows show the wind stress forcing at $t = 0$; The distributions of P^* (kN/m^2) and e are the same as for GYRE-0/W-OSS experiments (Fig. 4e,f).

about 0.4 m/s. The distribution of the P_{tr} shown in the middle panels of Fig. 7 has two clear maxima in the south with the magnitudes of about 70 and 50 kN/m^2. Note, that due to the ice convergence causing SIT growth, both P_{tr} maximuma increase in magnitude and slightly (60 km) move toward each other.

The first guess initial SIT/SIV conditions and data for the PIZ-OSSE were derived from the true solution in a similar way as for GYRE-0-OSSE. Similarly, we specify the first guess with P^*=27.5 kN/m^2, e=2, and the exact wind forcing. The optimization was conducted in two steps by first optimizing $\boldsymbol{C}_{ic}$ and then $\boldsymbol{C}_{rh}$.

Figure 8a,c shows SIT, and the difference between optimized and true SIV at t=3d after optmization of the initial conditions only. Interestingly, despite less spatial variations in wind forcing, optimization of the initial conditions does not allow accurate reconstruction of the SIV as we observed in the GYRE-0/W-OSSEs. The maximum errors in the eastern part of the domain are about 0.1 m/s and being comparable in the magnitude with regional velocities. The relative accuracy of the SIV reconstruction in the western part is slightly better, but is still considerably worse than in the previous OSSEs.
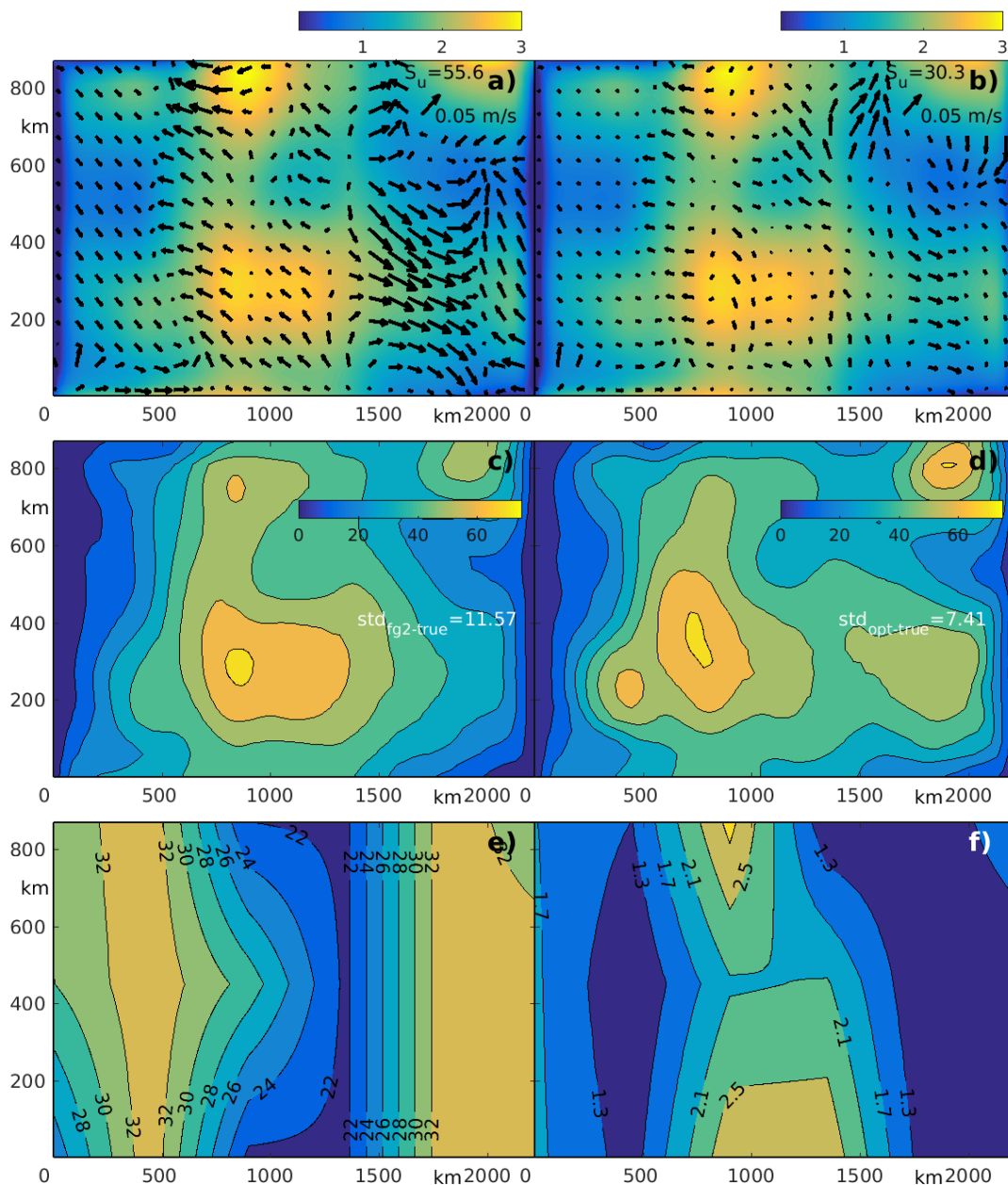
Figure 8. Results of the PIZ-OSSE: sub-optimal distributions of SIH (a) and P_{tr} (c) at t=3 d after optimizing the initial conditions $\boldsymbol{u}_0$, h_0, A_0 and the first guess values of P^*=27.5 kN/m^2 and e=2 The discrepancies $S_{\boldsymbol{u}}$ and S_{tr} with the true solutions and shown. Panels b and d: same as a and c, but after additional optimization of P^*, e; Bottom panels: optimized distribution of P^* (kN/m^2) and e. Black arrows show the difference between optimized and true SIV for each optimization stage.

The sub-optimal distribution of P_{tr} (Figure 8c) differs significantly from true P_{tr} (Figure 7d) both quantitatively and qualitatively. For example $std(P_{tr}^1(\text{opt})-P_{tr}(\text{true}))$ is 11.6 kN/m^2, or about 30-35% of the domain-average value of P_{tr}. The qualitative difference is probably more important because sub-optimal P_{tr} distribution fails to provide two maximuma discussed above. Instead, the sub-optimal distribution of P_{tr} has only one maximum located in the center (Figure 7d). This issue
370 is important because in realistic sea ice forecasts, improper prediction of P_{tr} may result for mechanical damage of ships due to extensive sea ice compression.

Additional optimization of the rheological parameters $\boldsymbol{C}_{rh}$ significantly improved the reconstructed SIV practically everywhere, so, the formal measure of the uncertainty S_u decreased almost two times from 56 m/s up to 30 m/s (Figure 8b). Similar improvements are visible in P_{tr} distribution (Figure 8d). The $std[P_{tr}^2(opt) - P_{tr}(true)]$ decreased to 7.4 kN/m^2 (by 40%) and
375 the fully optimized P_{tr} has two maxima as in the true P_{tr} distribution (Figure 7d).

The optimized P^* and e are shown at Figure 8e,f. In the eastern part of the model domain, the reconstructed P^* and e almost perfectly agree with the true distributions of P^* and e, while there is some difference between optimized and true rheology in western part. The effect could probably be attributed to the region with zero convergence along the western boundary, where the rheology does not play a significant role. There is also some quantitative difference between optimized and true e in the
380 central part of the model domain but qualitatively the reconstructed eccentricity has all features of the true e distribution.

5 Conclusions

The presented study continues our previous efforts (Stroh et al, 2019) and addresses the feasibility of retrieving spatially-varying RPs through the 4dVar assimilation the satellite observations of SIV, SIC and SIT. To do the analysis, we developed TLA codes with respect of all rheological parameters, initial conditions, and wind forcing for a single-category SIM recently
385 proposed by Lemieux et al., (2016). The dynamical core of this model is based on conventional formulation of the EVP rheology (Hunke and Dukowicz, 1997) and parameterizations of the grounding and arching land fast ice recently proposed by Lemieux et al., (2015, 2016) and Koning Beatty and Holland, (2010). The model was configured in multiple rectangular domains and included simplified advection numerical scheme.

It was found that TLA models for the EVP solver are unstable for the regions with high (>0.9) concentration and require
390 stabilization. The standard stabilization technique through the additional diffusion (Hoteit et al., 2005) widely used in the OGCM inverse modeling was found to be inefficient, but a simpler stabilization based on Newtonian friction appeared to work well. Analysis of the TL approximation accuracy has shown that Newtonian stabilization has errors similar to the ones observed in the case of diffusion-based stabilization, and thus the Newtonian scheme can be successfully used in SIMs based on the EVP solvers. At the same time, the simple analysis shows that the TLA model for the VP sea ice solver is stable
395 provided that forward model satisfies the stability criterion (which is always the case). We therefore conclude that SIMs with VP rheology (e.g. Hibler et al. (1979); Lemeaux et al. 2008) do not require additional stabilization of the TLA codes, and are formally more suitable for development of sea ice 4dVar DA algorithms.

In a comprehensive series of OSSEs with a simplified EVP sea ice model, it was demonstrated that Newtonian stabilization of the TLA codes allows reasonable reconstruction of the RPs. The numerical experiments included two series of the 4dVar

400 DA runs.

First, we analyzed the possibility of optimizing the RPs in two different LFI parameterization schemes incorporated in the CICE model (Hunke et al, 2010). In the current CICE6 version all LFI parameters are treated as spatially uniform variables, which degrades the accuracy of the LFI simulations in various parts of the Arctic Ocean (Lemieux et al., 2015), especially in the shallow sea and the narrow straits of the Canadian Archipelago. In this study, these parameters were specified by

405 spatially variable functions with a reduced number (10-15) of free parameters that were optimized to fit surface observations. The conducted OSSEs demonstrate that spatially varying LFI parameters k_2 and k_T, responsible for grounding and arching phenomena, can be optimized at a relatively low computational cost (5-12 iterations).

Taking into account that LFI typically forms in shallow/coastal areas and in narrow straits, the landfast phenomena can be controlled more efficiently by confining of the LFI controls to these areas in a high-resolution pan-Arctic SIM. It should

410 be noted that retrievals of the critical thickness parameter k_1 is not straightforward because of non-differentiability of the grounding parametrization scheme (eq. 2). Optimizing k_1 in the SIMs requires further development including more robust constrained minimization tools, such as genetic (Goldberg, 1989) or very fast simulation annealing (Ingber, 1989) algorithms.

In the second group of OSSEs, we analyzed the possibility of reconstructing spatially varying sea ice strength P^* and ellipse eccentricity e distributions. The respective OSSEs employed simulated observations of SIV and SIC characterized by RMSEs

415 of 0.025 m/s and 0.05 respectively, while SIT observations were simulated with uncertainties of 0.3 m, which is about two times smaller than the errors of the CryoSat-2 observations. The OSSEs also assessed sensitivity of the results with respect to systematic errors in wind forcing.

The OSSEs with accurate (exact) wind forcing demonstrated the feasibility of relatively accurate reconstruction of the P^* distribution and less successful, but still reasonable, reconstruction of the eccentricity field. Similar results were recently

420 obtained by Stroh et al (2019) who used 1d SIM featuring VP parameterization of the RPs, supporting a higher impact of the spatially varying P^* than e on the DA quality. We also observed that regions of less accurate P^* reconstructions are typically collocated with the regions of strong sea ice divergence and/or SIC concentrations below 0.8, i.e. with the regions where rheology plays a lesser role in sea ice dynamics.

We also found that additional optimization of P^* and e (after optimizing the initial state of sea ice) provides slightly more

425 accurate reconstruction of the SIT and SIC distributions and a significant improvement of the SIV and P_{tr} fields. Accurate forecasting of P_{tr} is very important because it better informs avoidance of regions with excessive compressive stress.

The OSSE with zonal wind convergence in the pack ice ($A=1$) demonstrated even better quality reconstruction of e and especially P^*. This can be attributed to a stronger impact of the internal stress on sea ice dynamics in pack ice. Similarly to the OSSEs with cyclonic wind pattern, we found that additional optimization of RPs provides smaller improvements in the SIT

430 and SIC hindcasts as compared to SIV and P_{tr}.

As mentioned above, this study utilized realistic observational errors for SIV and SIC, while SIT errors were twice smaller than the accuracy of currently available satellite observations. An additional set of experiments with more realistic SIT errors

reveals their stronger impact on the reconstruction quality of P^* and e, while the reconstruction accuracy of the LFI parameters k_2 and k_T remained virtually unchanged. The incoming satellite platforms (e.g. ICEsat-2, *https://icesat-2.gsfc.nasa.gov*) with a

435   better SIT observation capability may deliver sufficiently dense and accurate SIT observations required for reasonably accurate estimation of the P^* and e in the internal regions of the Arctic Ocean. Of particular importance are *in situ* SIT and other types of sea ice data that are currently planned to be collected in the framework of MOSAiC (*https://www.mosaic-expedition.org/*) experiment. These multi-variable and accurate atmospheric, oceanic, and sea ice observations should enable more accurate RPs estimation on the local scale through the 4dVar DA approach presented here. It is also noteworthy, that the extension of

440   the similar 4dVar DA based on the VP rheology may improve the accuracy of the reconstructed rheological parameters due to better stability of the TLA codes in the VP formulation. This extension, as well as more realistic inversions employing more complex rheological hypotheses (e.g., the Maxwell elasto-brittle rheology of Dansereau et al., (2016), could be within the focus of our studies in the near future.

Appendix A: On the stability of TL models with VP rheology

445   The VP system of equations is obtained by eliminating the time derivative in eq. (2), resolving the remainder with respect to $\boldsymbol{\sigma}$

$$\boldsymbol{\sigma} = \frac{1}{e^2}\left[\boldsymbol{P} - \boldsymbol{I}\frac{1-e^2}{2}\mathrm{tr}\boldsymbol{P}\right], \tag{A1}$$

and substituting (A1) into the momentum equation:

$$\tilde{\rho}hA(\partial_t + f\boldsymbol{k}\times)\boldsymbol{u} = \mathrm{div}\boldsymbol{\sigma} - \boldsymbol{\tau}_b + \boldsymbol{\tau}_a \tag{A2}$$

450

$$\partial_t h = \mathrm{div}(h\boldsymbol{u}) \tag{A3}$$

$$\partial_t A = \mathrm{div}(A\boldsymbol{u}) \tag{A4}$$

where we used the notation $\boldsymbol{P}$ for the tensor in the rhs of (2):

$$\boldsymbol{P} = P\left[(1+k_T)\frac{\varepsilon}{\Delta} - \frac{1-k_T}{2}\boldsymbol{I}\right] \tag{A5}$$

The non-linear system of VP equations (A1-A4) is solved in two stages. First, equation (A2) is stepped formward using a

455   semi-implicit scheme, which takes the fields of P and Δ from the previuos time step, treating only ε semi-implicitly. On the second stage, equations (A3-A4) are explicitly stepped forward in time using the velocity fields from the first stage (Hibler, 1979; Lemieux et al 2008).

   In application to TLA modeling, such procedure would not provide the exact derivative of the non-linear scheme with respect to $\boldsymbol{u}$ because equation (A2) is not linearized with respect to the variations of $\Delta(\boldsymbol{u})$ and will therefore exhibit behavior similar

460   to the behavior of the regularized code (Fig. 1). Moreover, exact TLA code of the VP rheology, is intrinsically unstable in the regions of ice divergence (e.g., Gray and Killworth, 1995), especially in the areas, where tensile stresses associated with arching effects are important.

However, one may expect reasonable performace of the above mentioned "incomplete linearization" of the VP model in the 4dVar applications, as soon as the stability criterion of the non-linear model (A1-A4) is satisfied. In that respect we may

465 conclude that VP rheology is less susceptible to the TLA instabilities than EVP, which requires introduction of the additional stabilization terms in the TLA code of the stress tensor evolution equation.

Author contributions. All authors provided substantial contribution to the models' development, interpretation of the results and writing the manuscript

Competing interests. The authors declare that they have no conflict of interest.

References

Allard, R. A., Sinead, L., Farrell, S. L., Hebert, D. A., Johnston, W. F., Li, L., et al. 2018: Utilizing CryoSat-2 sea ice thickness to initialize a coupled ice-ocean modeling system. Advances in Space Research,62(6), 1265-1280, https://doi.org/10.1016/j. asr.2017.12.030.

Cummings, J. A., and O. M. Smedstad, 2013: Variational data assimilation for the global ocean. In: Data Assimilation for Atmospheric, Oceanic and Hydrologic Applications (Vol. II), Springer, 303–343.

Dansereau V , J. Weiss, P. Saramito , and P. Lattes, A Maxwell elasto-brittle rheology for sea ice modelling, 2016: The Cryosphere, 10, 1339–1359, www.the-cryosphere.net/10/1339/2016/ doi:10.5194/tc-10-1339-2016.

Goldberg, D. E. 1989: Genetic Algorithms in Search, Optimization and Machine Learning, Addison-Wesley, Reading, MA, 432 pp.

Gray, J. M. N. T., and P. D. Killworth, 1995: Stability of viscous-plastic sea ice rheology, J. Phys. Oceanogr., 25(5), 971-978.

Fenty, I., D. Menemenlis, and H. Zhang, 2017: Global coupled sea ice-ocean state estimation. Climate Dynamics, 49 (3), 931–956.

Goldberg D.N and P.Heimbach, 2013: Parameter and state estimation with a time-dependent adjoint marine ice sheet model, The Cryosphere, 7, 1659–1678, www.the-cryosphere.net/7/1659/2013/ doi:10.5194/tc-7-1659-2013

Harder,M., and H. Fischer, 1999: Sea ice dynamics in the weddell sea simulated with an optimized model. Journal of Geophysical Research: Oceans, 104 (C5), 11 151–11 162.

Heimbach, P., 2008: The MITgcm/ECCO adjoint modelling infrastructure. Clivar Exchanges,44 (13), 1.

Hibler, W., 1979: A dynamic thermodynamic sea ice model. Journal of Physical Oceanography,9 (4), 815–846.

Hibler, W. D., and J. E. Walsh, 1982: On modeling seasonal and interannual fluctuations of arctic sea ice. Journal of Physical Oceanography, 12 (12), 1514–1523.

Hoteit, I., B. Cornuelle, A. Kohl, and D. Stammer, 2005: Treating strong adjoint sensitivities in tropical eddy-permitting variational data assimilation. Quart. J. Roy. Meteor. Soc., 131, 3659– 3682.

Hunke, E., and J. Dukowicz, 1997: An elastic–viscous–plasticmodel for sea ice dynamics. Journal of Physical Oceanography, 27 (9), 1849–1867.

Hunke, E. C. (2001), Viscous-plastic sea ice dynamics with the EVP model: Linearization issues, J. Comput. Phys., 170, 18–38.

Hunke, E. C., W. H. Lipscomb, A. K. Turner, N. Jeffery, and S. Elliott, 2010: CICE: the Los Alamos Sea Ice Model documentation and software users manual version 4.1 la-cc-06-012. T-3 Fluid Dynamics Group, Los Alamos National Laboratory, 675.

Ingber, L., 1989: Very fast simulated re-annealing, Math. Comput. Modelling, (12), 8, pp 967-973.

Komarov, A. S., and D. G. Barber, 2014: Sea ice motion tracking from sequential dual-polarization RADARSAT-2 images. IEEE Transactions on Geoscience and Remote Sensing, 52 (1), 121–136.

Kreyscher, M., M. Harder, and P. Lemke, 1997: First results of the Sea-Ice Model Intercomparison Project (SIMIP). Annals of Glaciology, 25, 8–11.

Kreyscher, M., M. Harder, P. Lemke, and G. M. Flato, 2000: Results of the sea ice model in tercomparison project: Evaluation of sea ice rheology schemes for use in climate simulations. Journal of Geophysical Research: Oceans, 105 (C5), 11 299–11 320.

Lemieux, J.-F., B. Tremblay, S. Thomas, J. Sedlacek, and L. A. Mysak, 2008: Using the preconditioned generalized minimum residual (GMRES) method to solve the sea-ice momentum equation. Journal of Geophysical Research: Oceans, 113 (C10).

Lemieux, J.F., Knoll, D., Tremblay, B., Holland, D., Losch, M., 2012. A comparison of the Jacobian-free Newton-Krylov method and the EVP model for solving the sea ice momentum equation with a viscous-plastic formulation: a serial algorithm study. J. Comp. Phys. 231, 5926–5944.

Lemieux, J.-F., L. B. Tremblay, F. Dupont, M. Plante, G. C. Smith, and D. Dumont (2015), A basal stress parameterization for modeling landfast ice, J. Geophys. Res. Oceans,120, 3157–3173, doi:10.1002/2014JC010678

515 Lemieux, J.-F., F. Dupont, P. Blain, F. Roy, G. C. Smith, and G. M. Flato, 2016: Improving the simulation of landfast ice by combining tensile strength and a parameterization for grounded ridges. Journal of Geophysical Research: Oceans, 121 (10), 7354–7368.

Losch, M., Fuchs, A., Lemieux,J.F., Vanselow, A., 2014: A parallel Jacobian-free Newton-Krylov solver for a coupled sea ice ocean model. J. Comp. Phys., 257, 901–911.

Massonnet, F., T. Fichefet, and H. Goosse, 2015: Prospects for improved seasonal Arctic sea ice predictions from multivariate data assimila-
520 tion. Ocean Modelling, 88, 16–25.

Menemenlis, D., J.-M. Campin, P. Heimbach, C. Hill, T. Lee, A. Nguyen, M. Schodlok, and H. Zhang, 2008: ECCO2: High resolution global ocean and sea ice data synthesis. Mercator Ocean Quarterly Newsletter, 31, 13–21. 32

Nichols N.K., 2003: Data Assimilation: Aims and Basic Concepts. In: Swinbank R., Shutyaev V., Lahoz W.A. (eds) *Data Assimilation for the Earth System*. NATO Science Series (Series IV: Earth and Environmental Sciences), vol 26. Springer, Dordrecht.

525 Nichols, N. K., 2010: Mathematical concepts of data assimilation. In: Lahoz, W., Khattatov, B. and Menard, R. (eds.) Data assimilation: making sense of observations. Springer, pp. 13-40. ISBN 9783540747024.

Nicolsky D.J, V.E. Romanovsky, G.G. Panteleev, 2009, Estimation of soil thermal properties using in-situ temperature measurements in the active layer and permafrost, Cold Regions Science and Technology (55) 120–129.

Schwegmann, S., C. Haas, C. Fowler, and R. Gerdes, 2011: A comparison of satellite-derived sea-ice motion with drifting-buoy data in the
530 Weddell Sea, Antarctica. Annals of Glaciology, 52 (57), 103–110. 35

Stroh J.N, G.Panteleev, M.Yaremchuk, O.Francis, R.Allard, 2019, Toward optimization of rheology in sea ice models through data assimila-
tion, in press JTECH

Sumata, H., R. Kwok, R. Gerdes, F. Kauker, and M. Karcher, 2015: Uncertainty of arctic summer ice drift assessed by high-resolution sar data. Journal of Geophysical Research: Oceans,120 (8), 5285–5301

535 Toyota, T., and N. Kimura, 2018: An examination of the sea ice rheology for seasonal ice zones based on ice drift and thickness observations. Journal of Geophysical Research: Oceans,123 (2), 1406–1428.

Tremblay, L.-B. and L.A.Mysak, 1997: Modeling sea ice as a granular material, including the dilatancy effect, J. Phys. Oceanogr., 27(11), 2342-2360.

Tremblay, L.-B., and M. Hakakian, 2006: Estimating the sea ice compressive strength from satellite derived sea ice drift and NCEP reanalysis
540 data. Journal of Physical Oceanography, 36 (11), 2165–2172. 2342-2360

Tschudi, M.,W. Meier, J. Stewart, C. Fowler, and J. Maslanik, 2019: Polar Pathfinder daily 25 km EASE-Grid sea ice motion vec-
tors, version 4 dataset 0116. NASA National Snow and Ice Data Center Distributed Active Archive Center, Boulder, CO USA,
doi:10.5067/INAWUWO7QH7B.

Vancoppenolle, M., T. Fichefet, H. Goosse, S. Bouillon, G. Madec, and M. A. M. Maqueda, 2009: Simulating the mass balance and salinity
545 of Arctic and Antarctic sea ice. 1. Model description and validation. Ocean Modelling, 27 (1-2), 33–53.

Wunsch,C.(1996),The Ocean Circulation Inverse Problem, 442 pp.,Cambridge Univ. Press, Cambridge

Yaremchuk, M., D.Nechaev, and G.Panteleev, 2009: A method of successive corrections of the control subspace in the reduced-order varia-
tional data assimilation. Mon. Wea, Rev., 137, 2966-2978.

Yaremchuk, M., and D. Nechaev, Covariance localization with diffusion-based correlation models, Mon. Wea. Review, (141), 848-860, 2013.

550 Yaremchuk, M., and P. Martin, On Sensitivity Analysis within the 4DVAR Framework, Mon. Wea. Review, (142), 774-787, 2014

Yaremchuk, M., Townsend, T., Panteleev, G., Hebert, D., and Allard, R. (2019). Advancing short-term forecasts of ice conditions in the Beaufort Sea. J.Geoph. Res.,124, 807–820. https://doi.org/10.1029/2018JC01458

Zhang, J., and D. Rothrock, 2003: Modeling global sea ice with a thickness and enthalpy distribution model in generalized curvilinear coordinates. Monthly Weather Review, 131 (5), 845–861.

555   Zhnag, Y-F., and C. M. Bitz, 2018: Insights on sea ice data assimilation from perfect model observing system simulation experiments, J. Clim., 31(8), 5911-5926.